Journal of Materials Chemistry A

ROYAL SOCIETY OF CHEMISTRY

PAPER

View Article Online
View Journal

Cite this: DOI: 10.1039/d6ta01893a

Efficient bubble removal in superhydrophilic gas diffusion electrodes *via* poly(vinyl alcohol) coating for high-current anion-exchange membrane water electrolysis

In-Ho Baek,†[a] Sang-Mun Jung, †[a] DoEun Kim,†[b] Jihyun Choi,[d] Jinwoo Baek,[a] Byung-Hun Lee,[a] Byung-Jo Lee,[a] Haeyong Shin,[a] Sang-Hoon You,[ef] Kyu-Su Kim,[g] Hyun S. Park, *[d] HangJin Jo*[bc] and Yong-Tae Kim *[a]

Received 4th March 2026
Accepted 4th May 2026

DOI: 10.1039/d6ta01893a

rsc.li/materials-a

Bubble-induced performance degradation caused by gas bubble accumulation, particularly at high current density, significantly hinders the performance of anion-exchange membrane water electrolysis (AEMWE). Herein, we present a simple and cost-effective strategy for enhancing mass transport in AEMWE: applying a hydrophilic polyvinyl alcohol (PVA) coating to carbon paper (CP) to create gas diffusion electrodes (GDEs). This simple and scalable GDE modification with enhanced hydrophilic and aerophobic properties promotes efficient bubble detachment and suppresses bubble-induced transport losses, resulting in improved GDE performance. The optimized PVA-coated GDE achieved a 35% improvement in cell performance compared to untreated bare CP GDEs, reaching a current density of 2.85 A cm^{-2} at 2 V. Additionally, the PVA-coated GDE exhibited sustained operational stability, maintaining stable operation for over 100 h. These findings offer a practical approach to mitigating bubble-induced performance degradation and highlight the importance of electrode-level transport engineering for high-performance AEMWE hydrogen production.

Introduction

The production of hydrogen through water electrolysis is fundamental to the transition to a carbon-neutral energy economy, with three leading technologies: polymer electrolyte membrane water electrolysis (PEMWE), alkaline water electrolysis (AWE), and anion-exchange membrane water electrolysis (AEMWE).[1] PEMWE is renowned for its high current density and responsiveness, making it ideal for integration with variable renewable energy sources; however, its reliance on expensive precious metal catalysts presents economic barriers.[2] Conversely, AWE, the most established water electrolysis technology, leverages nonprecious metal catalysts and robust designs for cost-effective, large-scale hydrogen production. Nevertheless, it operates at lower current densities and demonstrates slower adaptability to renewable energy fluctuations compared to PEMWE.[3,4] AEMWE has emerged as a compelling alternative, as it combines the cost-efficiency of AWE with the high performance of PEMWE and leverages cheaper catalysts while maintaining efficient hydrogen production.

The performance and operational efficiency of AEMWE are intricately governed by a combination of factors, including ohmic resistance, charge-transfer resistance, and mass-transfer resistance.[5] In gas-evolving AEMWE, however, a distinct form of transport-related loss arises from bubble-induced performance degradation, rather than from classical concentration polarization of reactants.[6] This bubble-induced performance degradation plays a critical role because it introduces an additional ohmic component known as bubble-induced resistance. This resistance occurs when gas bubbles accumulate within the electrolyte or at the interface between the electrolyte and the catalyst layer. These bubbles obstruct ion-conduction pathways and thus increase the ionic resistance, thereby increasing the high-frequency resistance (HFR).[7,8] As bubble accumulation progresses, the bubbles create localized "dead areas" on active

[a]Department of Materials Science and Engineering, Pohang University of Science and Technology, Pohang 37673, Republic of Korea. E-mail: yongtae@postech.ac.kr
[b]Department of Advanced Nuclear Engineering, Pohang University of Science and Technology, Pohang 37673, Republic of Korea
[c]Department of Mechanical Engineering, Pohang University of Science and Technology, Pohang 37673, Republic of Korea
[d]Center for Hydrogen-Fuel Cell Research, Korea Institute of Science and Technology (KIST), Seoul 02792, Republic of Korea
[e]Department of Mechanical and Automotive Engineering, Kongju National University, Cheonan, 31080, Republic of Korea
[f]Department of Future Convergence Engineering, Kongju National University, Cheonan, 31080, Republic of Korea
[g]Department of Mechanical Engineering, Dong-A University (DAU), Busan 49315, Republic of Korea
† I.-H. Baek, S.-M. Jung and D. Kim contributed equally to this work.

catalytic sites, which aggravates both ohmic and mass transport resistances and ultimately lowers the overall system efficiency.[9,10] While overcoming these bubble-induced performance degradation challenges is essential for advancing AEMWE technology to fulfill the demands of large-scale hydrogen production, most of the research has disproportionately focused on improving catalyst activity, leaving this challenge relatively less explored.

Efforts to address bubble-induced performance degradation have primarily centered on designing nanostructured catalysts. For the hydrogen evolution reaction (HER), aerophobic Ni nanorods have been developed to enhance hydrogen bubble detachment by leveraging their unique structural properties.[11] Similarly, MoS_2-based catalysts with hydrophilic surfaces have shown potential in facilitating bubble release and maintaining efficient reaction interfaces.[10] For the oxygen evolution reaction (OER), nickel–iron layered double hydroxide (NiFe LDH) monolayer structures have proven effective in improving oxygen bubble release.[12] Bifunctional catalysts, such as $Fe_{0.2}Ni_{0.8}P_{0.5}S_{0.5}$, have been explored to enhance mass transfer for both the HER and OER.[13] While these advancements are promising, their implementation in full-cell applications faces significant hurdles. In particular, synthesizing nanostructures with precise architectures and scaling them up for large-scale production remain significantly challenging. In contrast to catalyst-focused approaches, modifications to gas diffusion layers (GDLs), gas diffusion electrodes (GDEs), or bipolar plates offer a practical pathway to address bubble-induced performance degradation in water electrolyzer systems. Lee *et al.* developed nanochannel GDEs using femtosecond laser ablation to enhance both oxygen diffusion and water transport.[14] Huang *et al.* fabricated ordered Ni GDLs, commonly referred to as a porous transport layer, with straight-through pores and adjustable grid sizes *via* 3D printing technology, accelerating gas escape in water electrolyzers.[15] Yang *et al.* reported Au-coated stainless steel bipolar plates produced through selective laser melting, demonstrating superior mass transport properties.[16] While these strategies are effective, expensive manufacturing processes and the use of noble metals are often required. Moreover, such modifications may increase contact resistance between the catalyst layer and the GDL, necessitating careful optimization to balance these competing factors.[17,18]

In this study, we present a novel strategy for addressing bubble-induced performance degradation in AEMWE systems by engineering hydrophilic CPs through a simple and cost-effective polymer coating process (Scheme 1). This process enables precise control of the degree of hydrophilicity. The AEMWE performance was then systematically evaluated according to the hydrophilicity of the GDEs. Low-cost polyvinyl alcohol (PVA) polymer was employed as a hydrophilic coating material to modify carbon-based GDEs, enabling them to exhibit both hydrophilic and aerophobic properties. This innovative approach significantly improved bubble removal efficiency and minimized bubble-induced performance degradation. By optimizing the PVA coating level, we identified a condition that maximizes bubble-removal benefits while minimizing the transport limitations associated with excessive coating. These findings demonstrate the potential of polymer-coated GDEs for addressing bubble-induced performance degradation in AEMWE systems, highlighting their potential as a viable engineering approach for the development of high-performance water electrolyzers.

Results and discussion

Polymer selection for the hydrophilic CP

The polymer-screening protocol for the hydrophilic CP is visualized in Fig. 1. Several polymers, including PVA, polyvinylpyrrolidone (PVP), polyethylene glycol (PEG), polylactic acid (PLA), and polyamide (PA), were initially considered as potential candidates for hydrophilic polymers.[19] Hydrophilicity of polymers is governed by the functionalities on the backbone and side-chains. In general, polar motifs stabilize a bound water layer at the water-bubble interface (producing aerophobic behavior), whereas non-polar backbones yield hydrophobic, aerophilic surfaces. Accordingly, we first screened polymers by the polarity and hydrogen-bonding capacity of their backbone/side-chain functionalities. Within this framework, PVA (dense –OH groups; donor and acceptor), PVP (lactam amide C═O; strong H-bond acceptor), PEG (repeating ether –O–; H-bond acceptor), and PA (polyamide; –CONH– donor/acceptor) are intrinsically hydrophilic polymers. By contrast, hydrophobic polymers such as PP (hydrocarbon backbone with methyl side groups) and PU (urethane linkages embedded within long aliphatic/aromatic soft segments that dominate the surface) exhibit low effective surface polarity and therefore remain hydrophobic.[20–24]

Among the hydrophilic candidates, we first excluded PLA and PA due to insufficient chemical stability in alkaline aqueous media. PLA was ruled out because its ester linkages undergo alkaline hydrolysis (saponification) in aqueous media, particularly accelerated at elevated temperature, thereby resulting in poor long-term stability.[21] Although PA is hydrophilic, it exhibits substantial water uptake and swelling, and its amide bonds are also susceptible to alkaline hydrolysis at elevated temperature, limiting durability in concentrated KOH.[24]

Next, mechanical stability and interfacial adhesion under alkaline aqueous conditions guided the final polymer selection. PVP was excluded because the strong polarity of its lactam carbonyls renders it readily water-soluble at room temperature, without extensive crosslinking or covalent immobilization.[20,25] As a result, PVP films could be leached or dissolved during long-term AEMWE operation. PEG was excluded because its highly flexible chains act as an internal plasticizer, lowering cohesive energy density and weakening film integrity and adhesion under aqueous shear unless chemically bonded to the substrate.[22]

Based on this polymer-screening protocol, PVA was selected as the polymer for hydrophilic CPs. The high density of –OH groups enables strong interfacial interactions with common substrates (*e.g.*, metal oxides and oxygen-functionalized carbons), while an extensive interchain hydrogen-bond network yields cohesive, mechanically robust, and adherent films. These features maintain a strongly hydrophilic

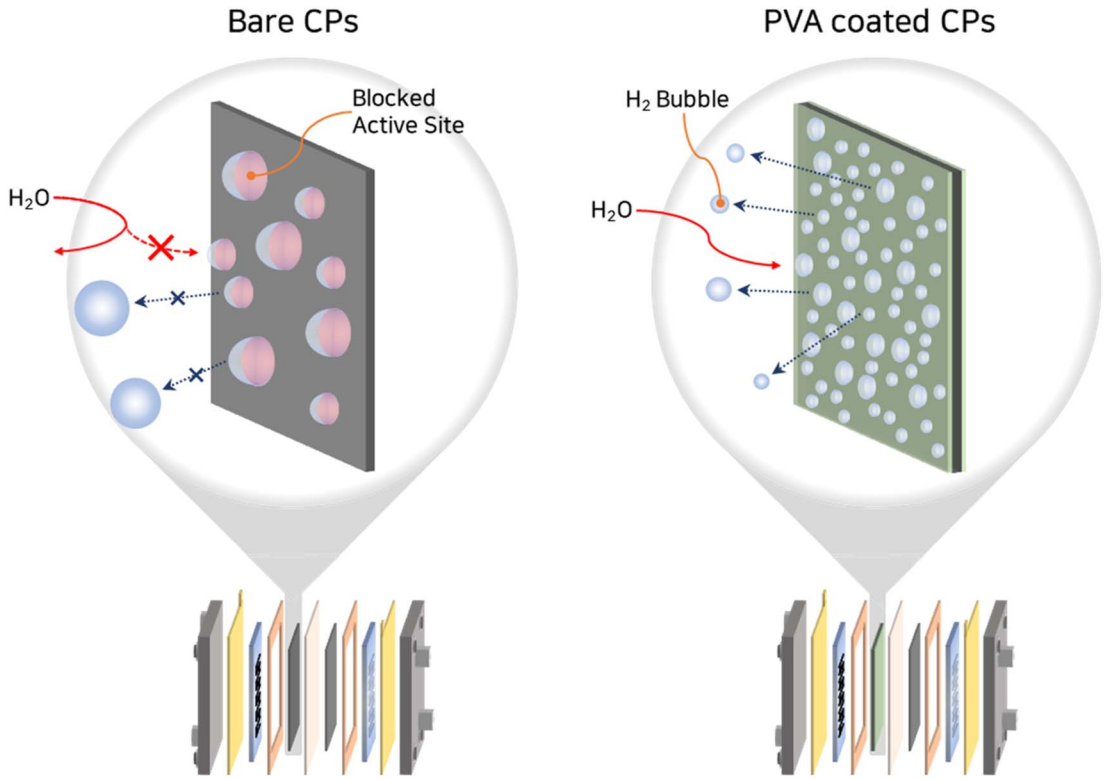

Scheme 1 Schematic of bubble dynamics on HER gas diffusion electrodes: bare GDE (left) *vs.* PVA-coated GDE (right).

(aerophobic) surface that sustains a bound hydration layer and mitigates gas-bubble adhesion, thereby improving moisture/water management.[26] In addition, PVA exhibits broad chemical resistance across acidic, alkaline, and many organic environments and provides adequate thermal stability (up to ~200 °C), supporting uniform coatings with high mechanical strength and long service life.[27,28] In practice, the degree of hydrolysis, molecular weight, and mild crosslinking can be tuned to increase water resistance and suppress polymer leaching under alkaline aqueous operation.[23] PVA also offers practical advantages, including environmental benignity, cost-effectiveness, and nontoxicity, making it suitable for durable hydrophilic coatings.[29] Table 1 provides a comparative summary of the properties of all the considered polymers. The initial screening of polymer candidates, as summarized in Fig. 1 and Table 1, was conducted by systematically evaluating their established physicochemical properties documented in the literature to identify the most suitable candidate for this study.

Material characterization of PVA-coated CP

The PVA-coated hydrophilic CPs were prepared using a dip-coating method, as illustrated in Fig. 2a. Specifically, PVA solutions with different weight percentages were prepared, and CP was immersed in them to achieve uniform coating on the CP surface. The uniformity of the PVA coating was confirmed through optical microscopy and scanning electron microscopy (SEM), which revealed no significant changes in the surface morphology after the PVA coating (Fig. S1 and S2). The coated samples were denoted as PVA-C4, PVA-C2, PVA-C1, PVA-C0.5, PVA-C0.25, PVA-C0.1, PVA-C0.05 and PVA-C0.025 based on the concentration of the PVA solutions used. The actual amount of retained PVA on the CP was quantified gravimetrically as areal mass loading from the sample weight difference before and after dip-coating, rinsing, and drying (Table S1). Fig. S3–S6 provide a schematic illustration, cross-sectional SEM images, and elemental mapping of the final catalyst-coated GDEs, clarifying the overall electrode architectures of both the PVA-coated and bare CP GDEs and the location of the Pt-containing catalyst layer.

The PVA coating on the CPs was confirmed using thermogravimetric analysis (TGA), as shown in Fig. 2b. The thermal decomposition profile of the PVA powder (dotted line) displayed three distinct stages of mass loss (Fig. S7). The initial stage, which occurred below 100 °C, was attributed to the evaporation of residual moisture. The second stage, which occurred between 250 °C and 350 °C, involved the decomposition of hydroxyl groups, resulting in the formation of water, aldehydes, and methyl ketones. The third stage, which occurred above 400 °C, involved the breakdown of the polyene structure into carbon and hydrocarbons.[30,31] All the PVA-coated CPs exhibited similar thermal decomposition patterns (Fig. 2b). The degree of weight loss correlated directly with the concentration of the PVA solution, confirming the successful deposition of PVA on the CP surface. The PVA coating was further confirmed through Raman spectroscopy (Fig. 2c). The Raman spectrum of the PVA powder exhibited the characteristic C–H stretching vibration peaks of PVA in the 2900–2950 cm^{-1} range[32] (Fig. S10). These vibration

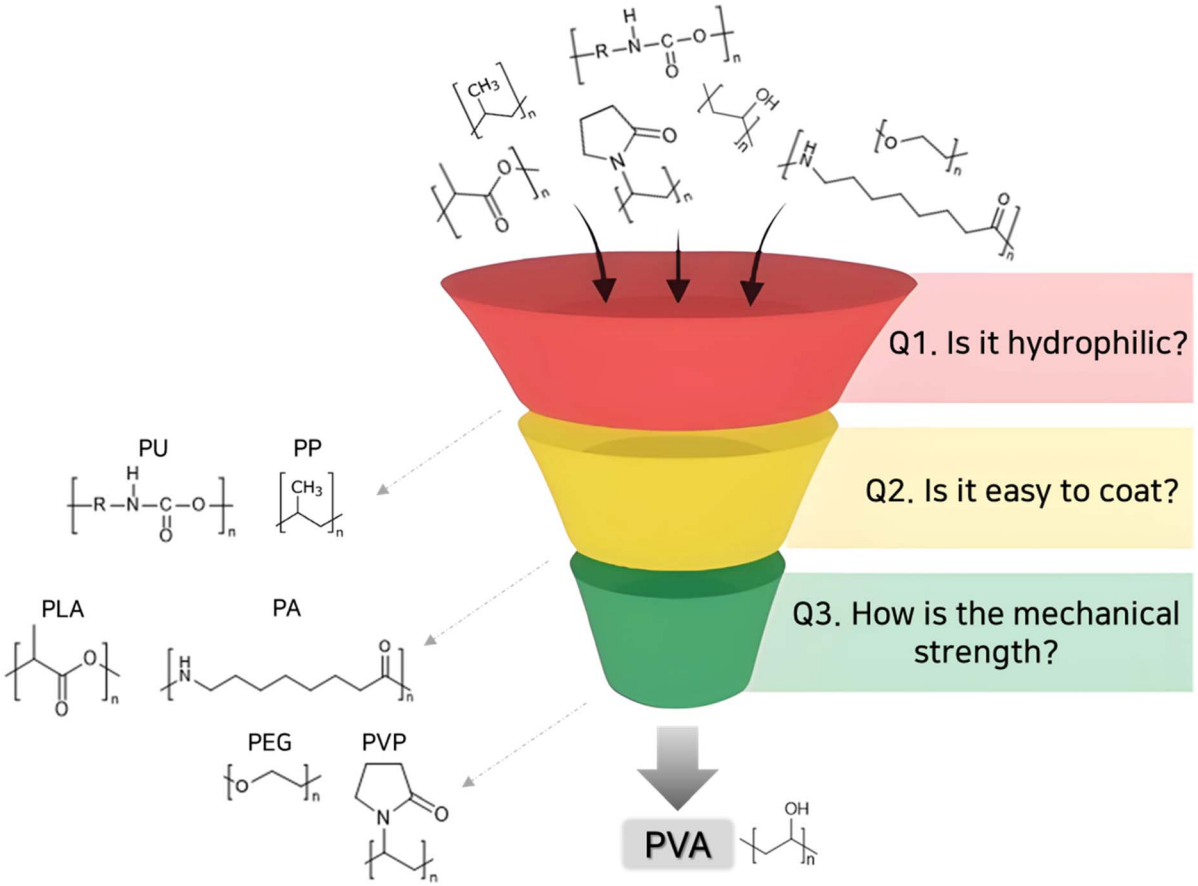

Fig. 1 Screening protocol for the hydrophilic CP.

peaks were also detected in the PVA-coated CPs, further confirming the successful deposition of the PVA layer on the CP surface.

The adhesion of the PVA coating to CP is likely assisted by hydrogen-bonding and other polar interfacial interactions. Carbon fiber surfaces can contain oxygen-containing functional groups, such as hydroxyl, carbonyl, and carboxyl groups.[33,34] The hydroxyl-rich PVA layer can interact with these sites and may also interact with polar groups in the ionomer, which is consistent with improved interfacial cohesion.[35–38]

Table 1 Comparison of the polymers for the hydrophilic CP. The scoring criteria are defined as follows: 'O' (excellent) indicates high suitability (*e.g.*, highly hydrophilic, robust chemical stability in alkaline media); '△' (moderate) indicates conditional suitability (*e.g.*, susceptible to excessive swelling or alkaline hydrolysis over time); 'X' (poor) indicates unsuitability (*e.g.*, inherently hydrophobic or highly soluble in water)

	PVA	PVP	PEG	PLA	PA	PP	PU
Name	Polyvinyl alcohol	Polyvinyl pyrrolidone	Polyethylene glycol	Polylactic acid	Polyamide (nylons)	Polypropylene	Polyurethane
Chemical formula	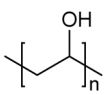	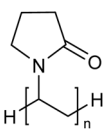	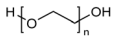	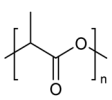	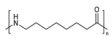	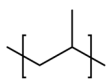	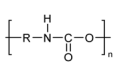
Hydrophilicity	O	O	O	△	△	X	X
Water solubility	O	O	O	△	X	X	O
Chemical stability	O	O	△	X	X	O	O
Thermal stability	O	O	△	△	△	O	O
Mechanical stability (adhesion)	O	△	X	△	△	O	O
Eco-friendliness	O	△	O	O	△	X	X

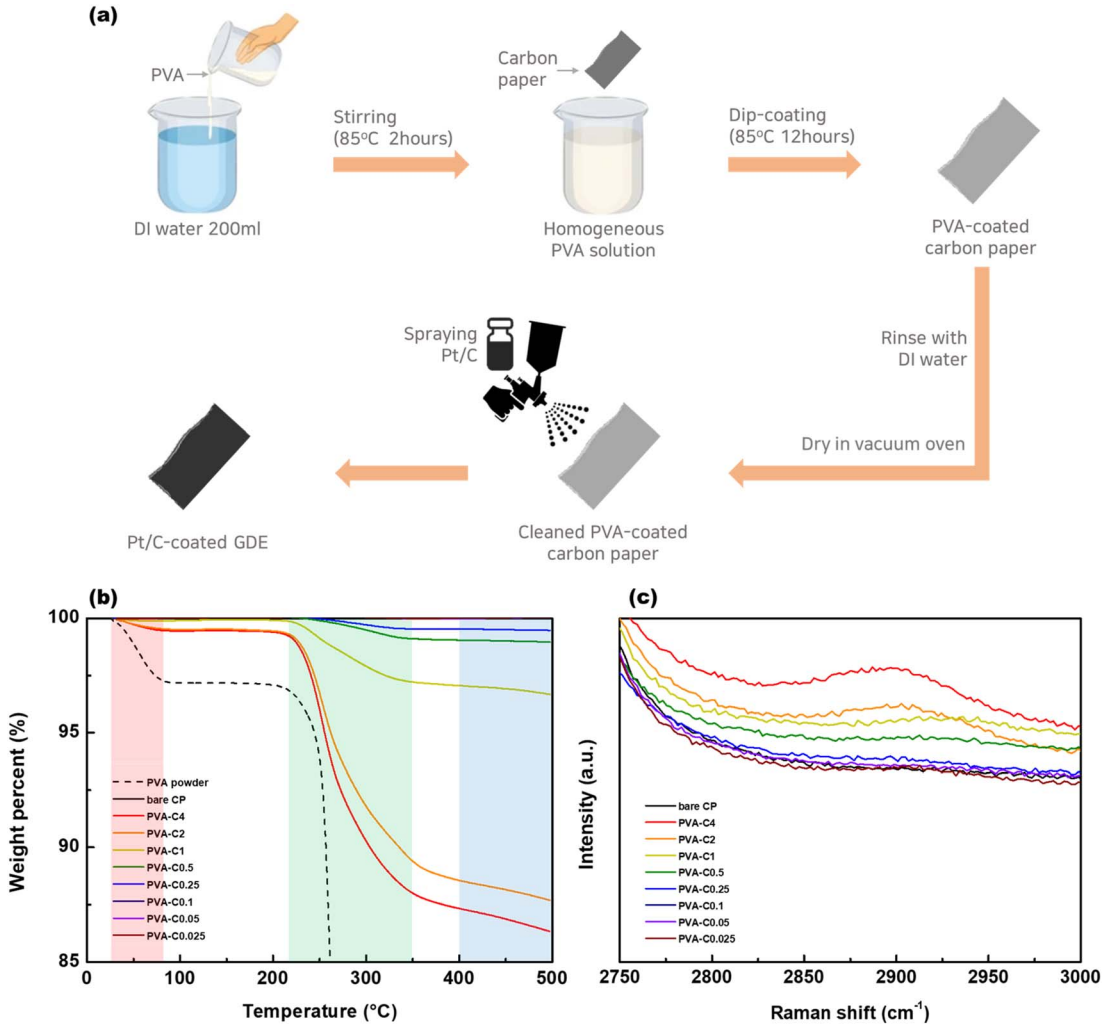

Fig. 2 (a) Schematic illustration of the PVA-coated CP synthesis process involving dip-coating. (b) TGA graph of the thermal decomposition profiles for the PVA-coated CPs and PVA powder. (c) Raman spectra of the PVA-coated CPs highlighting the characteristic C–H stretching vibration peaks.

Hydrophilic and aerophobic properties of PVA-coated CPs

The aerophobicity and hydrophilicity of the PVA-coated CP samples were compared to confirm their wettability. The aerophobicity, a critical parameter for evaluating wetting properties, was assessed by measuring the contact angle between air bubbles and the CP surface submerged in water. As shown in Fig. 3a, the bare sample exhibited a bubble contact angle of approximately 93°, whereas the PVA-C0.25 sample displayed a significantly higher bubble contact angle of 127°, indicating an enhanced aerophobic surface. Moreover, the aerophobicity of the PVA-coated CPs improved progressively as the PVA solution concentration increased (Fig. 3b). The PVA-C4 sample achieved the highest bubble contact angle of 134° (Fig. S11). These results confirm that the PVA coating significantly influenced the wettability of the CP.

The hydrophilicity of the PVA-coated CPs was also evaluated by measuring the contact angle between water droplets and the CP surface. The bare CP exhibited a water contact angle of approximately 120°, indicating that it had a hydrophobic surface. Conversely, PVA-C0.25 exhibited a water contact angle of 0° because it absorbed the water droplet instantaneously (Fig. 3c). This finding clearly demonstrates that the PVA coating significantly enhanced the hydrophilicity of the CP.

The hydrophilic and aerophobic properties of PVA-coated CPs contribute significantly to bubble removal during water electrolysis. To verify the bubble removal effect of PVA-coated GDEs, the behavior of H_2 gas bubbles during the HER was observed using a camera. A platinum-on-carbon (Pt/C)-coated GDE was fabricated by hand-spraying a Pt/C catalyst onto the PVA-coated CP, as illustrated in Fig. 2a. The performance was evaluated using a three-electrode system with chronopotentiometry at a current density of 400 mA cm^{-2}, and the rear of the GDE was captured during the operation. As shown in Fig. 3d, the bare Pt/C coated GDE generated relatively large bubbles (average size: 1.201 mm) that became trapped within it. In contrast, the Pt/C coated PVA-C0.25 facilitated the formation of relatively small bubbles (average size: 0.373 mm) and enabled the rapid removal of the generated hydrogen gas (Fig. S12). The

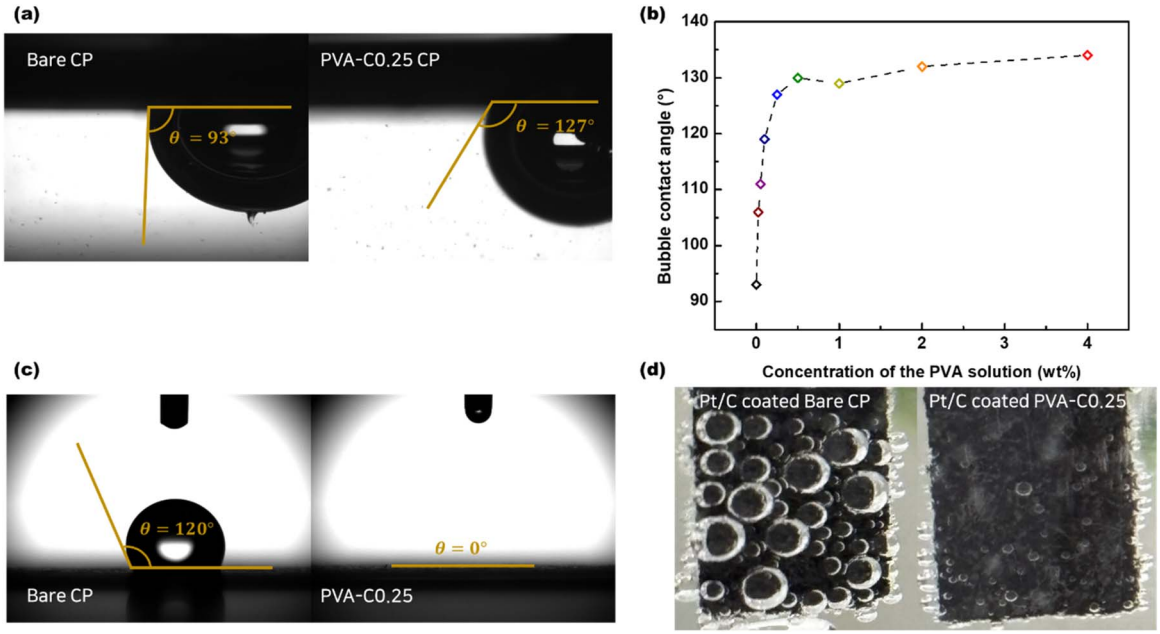

Fig. 3 (a) Contact angle measurement of air bubbles on the CP surfaces to assess aerophobicity. (b) Comparison of aerophobicity as a function of PVA coating solution concentration. (c) Contact angle measurement of water droplets on the CP surfaces to assess hydrophilicity. (d) Captured images of bubble formation on the GDE surfaces during the HER.

optical observations clearly demonstrate the improved bubble removal on PVA-coated GDEs.

To further elucidate these effects, scanning electrochemical microscopy (SECM) measurements were performed under HER operating conditions to provide quantitative and spatially resolved electrochemical insights beyond optical visualization. Although Nafion 212 was used in the SECM platform for experimental convenience, the SECM measurements were intended as a comparative probe to evaluate the relative interfacial gas-release behavior of bare GDE and PVA-coated GDE under identical local measurement conditions, rather than to reproduce the full membrane environment of the AEMWE cell. The measurements were performed in substrate-generation/tip-collection (SG/TC) mode, where a Pt ultramicroelectrode (UME) was biased for hydrogen oxidation reaction (HOR) while the GDE simultaneously operated for the HER. Using identical electrolytes and cell geometry, we directly compared the bare GDE and PVA-coated GDE at $j_{HER} = -50$ and -200 mA cm^{-2}. Fig. 4 presents the time-dependent HOR current measured at the UME during SG/TC operation over the bare and PVA-coated GDE substrates. The most noticeable difference between the two samples is the amplitude and frequency of current fluctuations. At both current densities ($j_{HER} = -50$ and -200 mA cm^{-2}), the UME signal above the PVA-coated GDE shows markedly smaller and more stable current variations, whereas the bare GDE exhibits large, irregular spikes. This trend is quantitatively supported by the current-fluctuation amplitudes summarized in Table S3. Such strong current oscillations over the bare GDE are consistent with transient perturbations of local H_2 transport near the interface, including intermittent blocking and release events associated with gas evolution. In contrast, the suppressed fluctuations above the PVA-coated GDE are consistent with a more stable local interfacial transport environment. Fast Fourier transform (FFT) analysis of the UME current further supports this interpretation, showing reduced low-frequency components for the PVA-coated surface, which is consistent with reduced low-frequency transport perturbations during gas evolution (Fig. S13 and S14).

It should be noted, however, that the SECM signal in the present SG/TC configuration is an indirect electrochemical probe of local H_2 transport rather than a direct measurement of bubble dynamics. In addition to gas evolution itself, the UME current response can also be influenced by changes in local diffusion paths, surface roughness/topography, and local hydrodynamic perturbations near the probe. Therefore, the SECM data alone do not uniquely determine absolute bubble size, bubble coverage, or detachment frequency. Instead, they provide a comparative indication that the interfacial transport environment above the PVA-coated GDE is more stable under otherwise identical measurement conditions. This interpretation is consistent with the direct optical observations of smaller bubbles and the improved wettability of the PVA-coated substrate.

Next, the differences in the time-averaged HOR current density and the corresponding collection efficiency further support the interpretation of more effective H_2 bubble release on the PVA-coated GDE. At both current densities ($j_{HER} = -50$ and -200 mA cm^{-2}), the PVA-coated GDE exhibits a lower mean HOR current density and consequently a smaller collection efficiency compared with the bare GDE (Table S2). Since the same HER current was applied, this decrease does not indicate reduced hydrogen generation but rather more efficient H_2

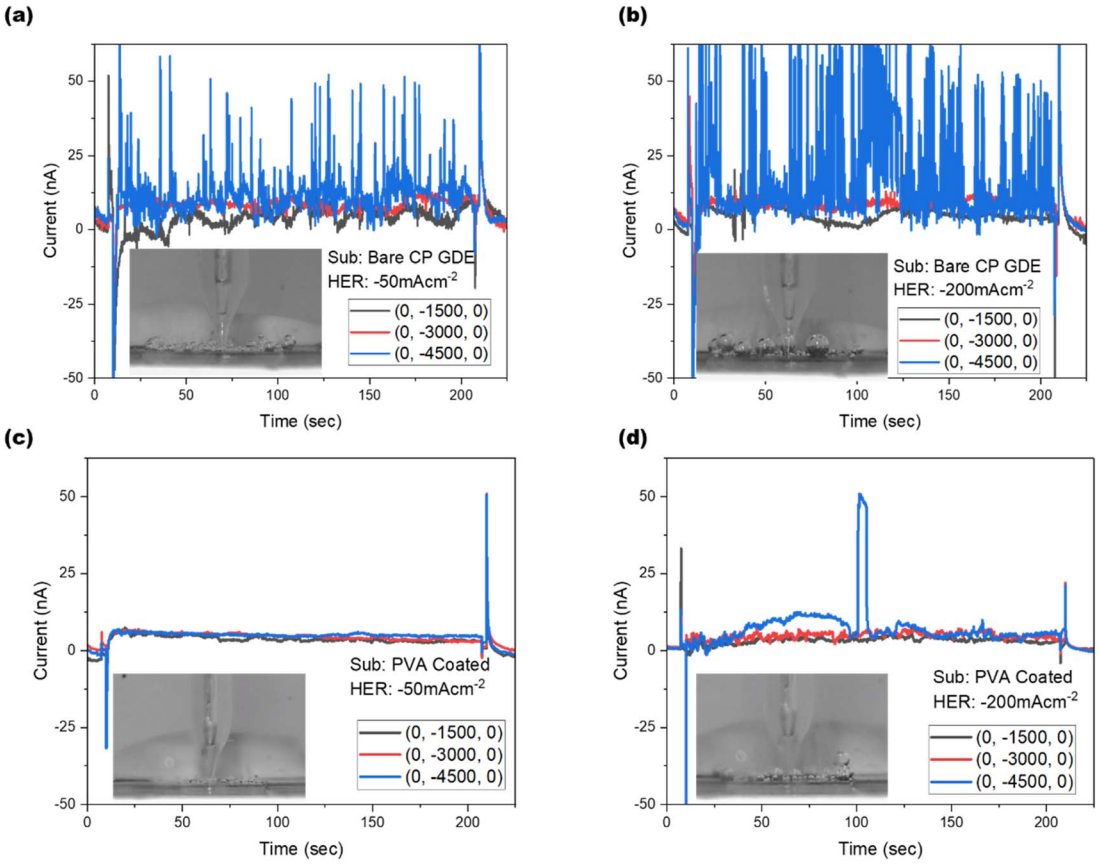

Fig. 4 HOR current density measured at the UME during SG-TC mode over bare CP GDE under the HER current density of (a) −50 mA cm^{-2} and (b) −200 mA cm^{-2} and over PVA coated GDE under the HER current density of (c) −50 mA cm^{-2} and (d) −200 mA cm^{-2}.

removal near the electrode surface. In the PVA-coated GDE, H_2 bubble growth is effectively suppressed and detachment occurs more rapidly, minimizing local H_2 accumulation and facilitating faster diffusion of H_2 away from the GDE.

Collectively, these results confirm that PVA-coated GDEs exhibit both aerophobic and hydrophilic surface properties, which significantly improve their wettability. This improved wettability contributes significantly to bubble removal during water electrolysis, as demonstrated by the rapid formation and detachment of small hydrogen gas bubbles during the HER performed in this study. This dual functionality of the PVA coating enhances bubble removal efficiency, improving the overall performance and operational efficiency of GDEs in AEMWE applications.

AEMWE performance of the PVA-coated GDE

The practical utility of the hydrophilic and aerophobic PVA-coated GDE was evaluated in an AEMWE system (Fig. 5a). The GDEs for the HER were fabricated by hand-spraying a Pt/C catalyst onto the PVA-coated CPs and a bare CP until a Pt loading of 0.2 mg_{Pt} cm^{-2} was achieved. To fabricate the OER GDEs, a synthesized NiFe LDH catalyst was applied *via* hand-spraying at a loading of 2 mg_{cat} cm^{-2}. Both GDEs were then assembled into an AEMWE cell using an FAA-3-50 membrane (Fumatech, 50 μm) that had been preconditioned in 1 M potassium hydroxide (KOH) for over 1 day.

Fig. 5b and S15 show the polarization curves of AEMWE cells operating under 1 M KOH conditions, comparing their performances based on different concentrations of the PVA coating solution (PVA-C0.05 to PVA-C4). As the concentration of the PVA coating solution increased, the AEMWE performance improved from the bare CP GDE to PVA-C0.25 (Fig. 5c). The optimal concentration of the PVA coating solution was determined to be 0.25 wt% (PVA-C0.25), as it achieved a current density of 2.85 A cm^{-2} at 2 V, which was ~35% higher than that achieved by the bare CP GDE (2.1 A cm^{-2}). These results emphasize that the aerophobic and hydrophilic properties of the GDEs significantly enhance AEMWE performance.

However, when the PVA solution concentration used for coating exceeded 0.25 wt% (*i.e.*, PVA-C0.5 to PVA-C4), the AEMWE performance began to decline, unlike in the case of PVA-C0.25 (Fig. 5c). Specifically, the AEMWE cell with PVA-C4 exhibited a current density of 2.27 A cm^{-2} at 2 V, which was approximately 25% lower than that of PVA-C0.25. To clarify this trend, we deconvoluted the overall cell voltage of bare GDE and PVA-C0.25 GDEs at the low current densities (<1 A cm^{-2}) into individual components, including thermodynamic, ohmic, kinetic, and mass-transfer overpotentials. Under low current-density conditions, the voltage contributions are dominated

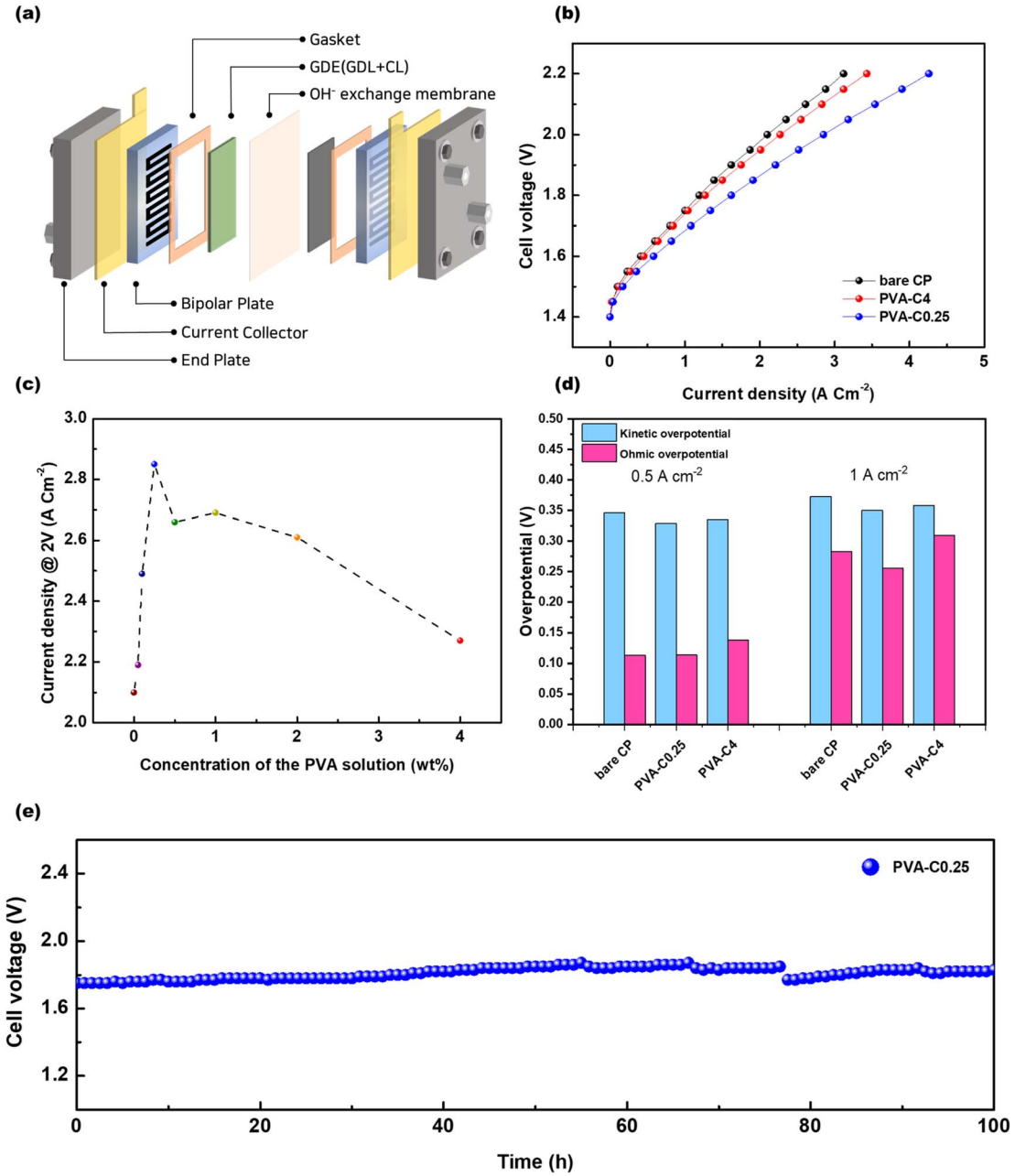

Fig. 5 (a) Schematic of the AEMWE cell. (b) Polarization curves of the AEMWE cells (black: bare CP GDE, red: PVA-C4, and blue: PVA-C0.25). (c) Current density at 2 V as a function of the PVA solution concentration. (d) Decoupled overpotentials of the AEMWE cells, categorized into kinetic and ohmic overpotentials. (e) Long-term stability test results of PVA-C0.25 at 1 A cm^{-2}.

by kinetic and ohmic terms, and the mass-transfer component remains negligible. At 0.5 A cm^{-2}, both bare CP GDE and PVA-C0.25 exhibit nearly identical ohmic and kinetic overpotential. This demonstrates that the dilute 0.25 wt% coating provides superhydrophilicity without forming a continuous insulating barrier. Due to the intrinsic surface roughness of the carbon fibers, sufficient physical contact points are preserved between the carbon asperities and the catalyst layer, thereby maintaining the electronic transport network. Only the PVA-C4 sample shows a slightly larger ohmic overpotential, indicating that an additional transport-related penalty emerges at excessive PVA loading. As discussed below, this trend is more consistently explained by hindered bubble evacuation through the porous network than by bulk electronic resistance alone. Beyond 1 A cm^{-2}, however, the bare CP GDE displays a pronounced increase in the total overpotential, driven primarily by an increased ohmic component arising from gas-bubble accumulation within the porous network. In contrast, the PVA-C0.25 GDE maintains a substantially lower ohmic overpotential over the entire current range compared to bare CP GDE, indicating more efficient bubble detachment and sustained electrolyte-filled conduction pathways. This decoupling analysis

quantitatively shows that the PVA coating mitigates bubble-induced ohmic blockage rather than conventional mass-transfer resistance. Accordingly, mass-transfer overpotentials are not the dominant factor at >1 A cm^{-2}, whereas bubble-related ohmic losses become increasingly significant at higher current densities (Fig. 5d and S16).

To understand why the ohmic loss decreases from bare CP to PVA-C0.25, we next examined the bubble nucleation and detachment behavior. Hydrogen bubble generation in the AEMWE occurs through a heterogeneous nucleation process on the electrode surface. In this mechanism, a geometric factor $f(\theta_b)$ – where θ_b is the bubble-side contact angle and $f(\theta_b)$ has a value between 0 and 1 – is incorporated into the homogeneous nucleation model to account for the reduction in the energy barrier caused by the presence of a solid surface, as illustrated in Fig. S17(a) (Note S2).[39] As the PVA coating concentration increases, the surface becomes more aerophobic. This aerophobic characteristic causes a larger bubble contact angle as observed in Fig. 3(b) and S11. Consequently, the nucleation free-energy barrier as shown in Fig. S17(b) rises with increasing PVA coating concentration thereby suppressing of bubble nucleation. Once a nucleus is formed, the bubble grows on the electrode surface until the buoyant force acting on it equals the adhesive force caused by surface tension. This force balance defines the bubble departure diameter described in Fig. S18 and Note S3. As the PVA coating concentration increases up to PVA-C0.25, the bubble detachment diameter decreases, indicating facilitated bubble release. Assuming that the projected bubble coverage scales with the square of the bubble detachment diameter, the coverage of PVA-C0.25 is estimated to be substantially lower than that of bare CP (Note S4). These results suggest that the reduced ohmic loss of PVA-C0.25 originates mainly from reduced bubble coverage and more effective preservation of electrolyte-filled ionic conduction pathways.

To clarify why the performance declines again beyond PVA-C0.25, we then analyzed the pore structure of the coated CP using mercury intrusion porosimetry (MIP). The bare CP exhibited a median pore diameter of 28.55 μm and a total intrusion volume of 2.3877 mL g^{-1}, whereas the optimized PVA-C0.25 sample showed similar values of 28.45 μm and 2.1064 mL g^{-1}, indicating that the dilute coating largely preserves the original porous transport network. In contrast, PVA-C4 exhibited a reduced median pore diameter of 26.05 μm and a lower total intrusion volume of 1.7910 mL g^{-1}. When pores larger than 25 μm are taken as macroporous gas-release pathways, the integrated macropore volume fraction remains nearly unchanged from bare CP to PVA-C0.25 but decreases for PVA-C4 (Fig. S19, Table S4 and Note S4). In addition, the reduced pore radius in PVA-C4 increases the relative capillary barrier for bubble passage through the porous network, which would further hinder bubble evacuation (Note S4). These results indicate that although the improvement in surface aerophobicity is nearly saturated beyond PVA-C0.25, excessive PVA loading reduces the accessible porous pathways for gas removal and increases the resistance to bubble passage through the GDE.

Finally, to determine whether the decline beyond PVA-C0.25 could instead originate from reduced bulk electronic conductivity, we analyzed the *ex situ* conductivity trend (Fig. S20) and estimated its corresponding voltage contribution (Note S5). Although the conductivity decreases at higher PVA loading, the calculated additional voltage loss is on the order of 10^{-5} V, which is far too small to explain the observed increase in ohmic loss by itself. Therefore, the performance decline beyond PVA-C0.25 is more appropriately interpreted as arising primarily from hindered bubble evacuation and the resulting increase in bubble-induced ohmic resistance, while the contribution from bulk electronic resistance is secondary.

Finally, the PVA-coated GDEs maintained their AEMWE performance for 100 h and showed no significant increase in overpotential during operation. This supports the operational stability of the PVA-coated GDE (Fig. 5e). Moreover, the aerophobic and hydrophilic GDE enabled efficient bubble release and minimized bubble accumulation inside the AEMWE cell. As a result, the system achieved stable and continuous operation through effective bubble management. A comparison with representative bubble-management strategies reported for AEMWE and closely related water-electrolysis systems is provided in Table S5. Collectively, these findings highlight the potential of PVA-coated GDEs to facilitate effective bubble management at the catalyst layer and GDL interface in AEMWE systems when coated with an appropriate concentration of PVA. This improvement enhances the overall performance of AEMWE systems through their hydrophilic and aerophobic properties. To further assess the stability of the PVA-coated GDE after long-term AEMWE operation, post-mortem SEM, elemental mapping, and wettability analyses were performed. The post-test SEM and EDS results (Fig. S21 and S22) remain comparable to the fresh-electrode data (Fig. S3–S6), showing no obvious structural collapse, catalyst-layer delamination, or major redistribution of the Pt-containing catalyst layer. Although the ultrathin PVA coating is not directly resolved as a distinct SEM layer because of its conformal and low-contrast nature, the post-test PVA-coated GDE still shows markedly improved wettability relative to the bare CP GDE (Fig. S23), indicating that the hydrophilic surface functionality is largely retained after durability testing.

Conclusion

In this study, we developed a novel strategy for addressing bubble-induced performance degradation in AEMWE systems by engineering GDEs with hydrophilic and aerophobic properties through PVA polymer coating. PVA was identified as the most suitable material because of its hydrophilic nature, robust adhesion, chemical resistance, and cost-effectiveness. A simple dip-coating process was employed to fabricate PVA-coated CPs with different PVA concentrations, enabling the precise optimization of bubble-removal benefits while avoiding transport limitations associated with excessive coating. The PVA coating enhanced the wettability of the CPs and increased the nucleation energy barrier, which suppressed bubble formation. It also weakened the adhesion between the bubble and the surface

so the bubble detached at a smaller diameter. Therefore, the amount of hydrogen bubble accumulation inside the AEMWE decreased during operation. Among the tested configurations, the PVA-C0.25-coated GDE demonstrated the most favorable balance between enhanced bubble removal and preserved porous transport pathways, achieving a current density of 2.85 A cm^{-2} at 2 V and a 35% improvement in performance compared to bare CP. The long-term stability of the PVA-coated GDEs was validated through extended operation over 100 h, confirming their stable operation under continuous operational conditions. These findings underscore the potential of PVA-coated GDEs to address bubble-induced performance degradation in AEMWE systems, offering a scalable and cost-effective strategy for enhancing the performance of hydrogen production technologies.

Materials and methods

Synthesis of the PVA-coated CP

The PVA-coated CP was synthesized by preparing PVA (M_W: 89 000–98 000, Sigma) solutions. PVA was dissolved in 200 mL of deionized (DI) water (18.2 MΩ cm) at concentrations ranging from 0.05 wt% to 4 wt% and stirred at 85 °C for 2 h. Subsequently, CP (AvCarb, MGL190, 2 cm × 5 cm) was uniformly coated *via* dip-coating by immersing it in the prepared PVA solution at 85 °C for 12 h.[40] Finally, the coated CP was rinsed with DI water to remove any residual PVA and then dried in a vacuum oven at 25 °C for 12 h. The actual amount of retained PVA on each coated CP sample was determined gravimetrically from the sample weight difference before and after dip-coating, rinsing, and drying, and the value was normalized by the geometric area of the substrate to obtain the areal mass loading (mg cm^{-2}).

Synthesis of NiFe LDH

NiFe LDH was synthesized using a previously reported method.[41,42] Nickel nitrate hexahydrate ($Ni(NO_3)_2 \cdot 6H_2O$; 45 mmol, Sigma), iron nitrate nonahydrate ($Fe(NO_3)_3 \cdot 9H_2O$; 15 mmol, Sigma), and urea (300 mmol, Sigma) were dissolved in 200 mL of DI water and stirred for 1 h. The pH of the mixture was adjusted to approximately 10.0 using a 1 M sodium hydroxide solution prepared with 97.0% sodium hydroxide (pellets, Sigma). After an additional hour of stirring, a coprecipitation reaction was conducted by heating the mixture at 100 °C for 20 h. After the reaction, the precipitate was washed with DI water and absolute ethanol (>99.5%, Daejung) three times each before being separated through centrifugation. The final product was dried in a vacuum oven at 60 °C for 24 h.

GDE fabrication and cell configuration

The gas diffusion electrodes (GDEs), defined here as the catalyst-coated GDLs, were prepared by spraying the catalyst ink onto either the bare CP or the PVA-coated CP substrates. To fabricate the cathode GDE, 0.25 g of Pt/C (46.9 wt%, TEC10E50E, Tanaka Kikinzoku Kogyo K. K.) was dispersed in a 15 mL mixture of DI water and isopropyl alcohol (IPA) (DI water : IPA volume ratio = 1 : 2). An ionomer solution (0.795 mL, I/C ratio of 0.6, FAA-3-10-solut, Fumatech) was added to the dispersion, which was then sonicated for 1 h to ensure proper dispersion. After sonication, the ink was manually sprayed onto CP, achieving a platinum loading of 0.2 mg_{Pt} cm^{-2}. To fabricate the anode GDE, 0.3 g of the NiFe LDH catalyst was dispersed in a 15 mL mixture of DI water and IPA, to which 0.4 mL of FAA-3-10 solution was added. This mixture was sonicated for 1 h and then hand-sprayed onto CP, achieving a total catalyst loading of 2 mg_{cat} cm^{-2}.

The FAA-3-50 membrane (Fumatech, 50 μm) was pretreated by immersing it in a 1 M KOH (Daejung) solution for 24 h and then transferring it to a fresh 1 M KOH solution for an additional 24 h. The membrane was thoroughly rinsed with DI water immediately before the cell assembly.

Evaluation of bubble removal from the GDEs using a three-electrode system

Electrochemical tests were conducted using a three-electrode system to evaluate bubble removal from the GDEs. The PVA-C0.25 GDE and bare GDE were used as the working electrodes, with Pt/C spray-coated onto their surfaces. A Hg/HgO electrode was used as the reference electrode, and a platinum wire served as the counter electrode. The bubble dynamics were observed under HER conditions in a 1.0 M KOH electrolyte. Electrochemical measurements were conducted using an electrochemical workstation (Metrohm Autolab PGSTAT204) with chronopotentiometry at a constant current density of 400 mA cm^{-2}. The rear of the GDE was imaged during the HER to monitor the bubble evolution.

The bubble size distribution was quantitatively analyzed using ImageJ software. The electrode surface area was used as a reference to calibrate the scale of each bubble image. The diameters of individual bubbles were measured by the program, and the data were compiled into a histogram to illustrate the bubble size distribution. The average bubble size was calculated from the measurements, providing a numerical representation of the bubble evolution during the HER.

Scanning electrochemical microscopy (SECM)

SECM measurements were conducted using a commercial scanning electrochemical microscope (M470, Bio-Logic SAS) equipped with a 25 μm Pt ultramicroelectrode (Pt UME, Bio-Logic, U-P5/25, RG ≈ 10). Prior to each experiment, the Pt UME was mechanically polished with alumina suspensions and aligned by recording approach curves in an aqueous solution containing 5 mM $K_3Fe(CN)_6$ and 1 M KCl. The working electrodes for SECM were fabricated following the same procedure used for the gas diffusion electrodes (GDEs), cut into 1.0 × 1.3 cm^2 rectangles, a Nafion 212 membrane (Chemours) was laminated onto the electrode by hot-pressing at 120 °C for 3 min. Nafion 212 was strategically selected as the laminated membrane for SECM measurements to facilitate the experimental setup, particularly for its superior thermal stability and ease of processing during the hot-pressing procedure. This configuration was specifically designed to guide the evolved gas

toward the back side of the GDL, thereby enabling clearer observation of the local interfacial electrochemical environment. During alignment, a negative feedback SECM curve was obtained over the area covered with a 60 μm Kapton film by measuring the $[Fe(CN)_6]^{3-}/[Fe(CN)_6]^{4-}$ reduction current at $-0.25\ V_{SCE}$ as the tip approached the insulated substrate. Based on the negative feedback curve, the tip-to-substrate distance (d) was fixed at 50 μm, corresponding to an i_{tip}/i_{bulk} ratio of 0.88. The d values from negative feedback modes was finally determined by fitting the experimental approach curves to the calculated theoretical curve.

$$I_T(L) = i_{tip}/i_{bulk} = 1/[A + B/L + C_{exp}(D/L) + (EL/F + L)] \text{ for negative feedback}$$

where $A = 0.45718$, $B = 1.46042$, $C = 0.43127$, $D = -2.35067$, $E = -0.14544$, and $F = 5.576$ for RG = 10.[43]

Under these fixed measurement conditions, the SECM response in SG/TC mode was used as a comparative probe of local interfacial H_2 transport. The measured tip current reflects the accessibility of electrochemically generated H_2 to the Pt UME, but it can also be affected by the local geometry of the interface and transport conditions near the probe. Therefore, the SECM measurements were used here to compare relative differences between bare and PVA-coated GDEs rather than to directly quantify absolute bubble size or detachment frequency.

AEMWE single-cell test

Anion-exchange membrane water electrolyzer single cells were tested at 50 °C. A 1 M KOH solution was circulated through both the anode and cathode compartments at a flow rate of 10 mL min^{-1} using an MPP20 pump (Maxclever, 3 V). A DC power supply (EX20-240, ODA Technology) was connected to the cell for voltage application. The polarization curve was obtained by performing a voltage sweep from 1.4 V to 2.2 V in 50 mV increments. Durability testing was conducted using chronopotentiometry at a constant current density of 1 A cm^{-2}.

Galvanostatic EIS and overpotential loss decoupling (AEMWE)

EIS was carried out on the assembled AEMWE cell using an electrochemical workstation (Metrohm Autolab PGSTAT204) with Booster 10A (Metrohm Autolab). The cell was first stabilized at 10 mA cm^{-2}, then EIS was recorded under load at 10, 25, 50, 75, 100, 150, 200, 300, 400, 500, 600, 700, 800, 900, 1000 mA cm^{-2}. Each step was held 3 s before acquisition. The frequency was swept from 10 kHz down to 10 Hz using NOVA software.

The high-frequency resistance (HFR) was obtained from the real-axis intercept of the Nyquist plot (or from the 10 kHz magnitude/phase fit when the intercept was ambiguous). Ohmic loss was computed as $\eta_{ohmic} = i \times HFR$

After iR-correction, the activation loss in the 10–50 mA cm^{-2} region was fitted to the Tafel relation

$$\eta_{act} = a + b\log\left(\frac{i}{i_{ref}}\right)$$

For pragmatic loss decoupling, we fixed a reference current density of 25 mA cm^{-2} (denoted i_{ref}). Using the fitted Tafel slope (denoted b), the activation loss was calculated.

Material characterization

TGA was conducted using a TGA/DSC thermogravimeter (SDT Q600 V20.9 Build 20). The PVA-coated CPs were heated from room temperature to 500 °C at 1 °C min^{-1} in an Ar atmosphere, and the changes in their weight were recorded. The morphologies of the PVA-coated CPs were observed using field-emission SEM (FE-SEM; JEOL FE-SEM-7100) and optical microscopy (OLYMPUS, BX21). Raman spectroscopy (Nano Photon, RAMAN WALK) was performed over a range of 50–3700 cm^{-1} to determine the presence of PVA in the PVA-coated CP.

The contact angle of water droplets was measured using a contact angle meter (SmartDrop_Plus, FEMTOBIOMED Inc.). A 6–7 μL droplet of water was placed on the bare CP and the PVA-coated CP samples that were synthesized with various PVA concentrations, and the contact angle was recorded. To measure the contact angle of air bubbles, a tank was filled with DI water, and the CP samples were suspended upside-down in it. Air bubbles (diameters: 5–10 μm) were introduced to adhere to the sample surfaces, and the resulting contact angle was observed.

Author contributions

In-Ho Baek: conceptualization, methodology, investigation, formal analysis, visualization, writing – original draft. Sang-Mun Jung: methodology, investigation, validation, formal analysis, writing – review & editing. DoEun Kim: investigation, formal analysis, resources. Jihyun Choi: investigation, validation, formal analysis. Jinwoo Baek: investigation, validation. Byung-Hun Lee: resources, investigation. Byung-Jo Lee: investigation. Haeyong Shin: investigation. Sang-Hoon You: resources, investigation. Kyu-Su Kim: formal analysis, visualization, writing – review & editing. Hyun S. Park: supervision, resources, writing – review & editing. HangJin Jo: conceptualization, supervision, project administration, funding acquisition, writing – review & editing. Yong-Tae Kim: conceptualization, supervision, project administration, funding acquisition, writing – review & editing.

Conflicts of interest

Authors declare that they have no competing interests.

Data availability

The data that support the findings of this study are provided in the manuscript and supplementary information (SI). Supplementary information: Fig. S1–S23, Notes S1–S5, and Tables S1–S5 providing additional material characterization. See DOI: https://doi.org/10.1039/d6ta01893a.

Acknowledgements

This work was supported by the National Research Foundation of Korea (NRF) grant funded by the Korea government (MSIT) (RS-2025-02303249 and 2022R1A2C3007855).

References

1 D. Li, E. J. Park, W. Zhu, Q. Shi, Y. Zhou, H. Tian, Y. Lin, A. Serov, B. Zulevi, E. D. Baca, C. Fujimoto, H. T. Chung and Y. S. Kim, *Nat. Energy*, 2020, **5**, 378–385.
2 N. Du, C. Roy, R. Peach, M. Turnbull, S. Thiele and C. Bock, *Chem. Rev.*, 2022, **122**, 11830–11895.
3 B.-J. Lee, S.-M. Jung, G. Yu, H.-Y. Kim, J. Kwon, K.-S. Kim, J. Kwak, W. Lee, D. H. Mok and S. Back, *ACS Catal.*, 2025, **15**, 1123–1134.
4 S. M. Jung, Y. Kim, B. J. Lee, H. Jung, J. Kwon, J. Lee, K. S. Kim, Y. W. Kim, K. J. Kim and H. S. Cho, *Adv. Funct. Mater.*, 2024, 2316150.
5 A. J. Bard, L. R. Faulkner and H. S. White, *Electrochemical Methods: Fundamentals and Applications*, John Wiley & Sons, 2022.
6 R. Iwata, L. Zhang, K. L. Wilke, S. Gong, M. He, B. M. Gallant and E. N. Wang, *Joule*, 2021, **5**, 887–900.
7 J. K. Lee, C. Lee, K. F. Fahy, P. J. Kim, J. M. LaManna, E. Baltic, D. L. Jacobson, D. S. Hussey, S. Stiber and A. S. Gago, *Energy Convers. Manage.*, 2020, **226**, 113545.
8 C. C. Weber, J. A. Wrubel, L. Gubler, G. Bender, S. De Angelis and F. N. Buchi, *ACS Appl. Mater. Interfaces*, 2023, **15**, 34750–34763.
9 M. Bühler, P. Holzapfel, D. McLaughlin and S. Thiele, *J. Electrochem. Soc.*, 2019, **166**, F1070–F1078.
10 Z. Lu, W. Zhu, X. Yu, H. Zhang, Y. Li, X. Sun, X. Wang, H. Wang, J. Wang and J. Luo, *Adv. Mater.*, 2014, **26**, 2683–2687.
11 J. Kim, S. M. Jung, N. Lee, K. S. Kim, Y. T. Kim and J. K. Kim, *Adv. Mater.*, 2023, **35**, 2305844.
12 S. S. Jeon, J. Lim, P. W. Kang, J. W. Lee, G. Kang and H. Lee, *ACS Appl. Mater. Interfaces*, 2021, **13**, 37179–37186.
13 L. Wan, Z. Xu, P. Wang, P.-F. Liu, Q. Xu and B. Wang, *Chem. Eng. J.*, 2022, **431**, 133942.
14 J. K. Lee, F. Babbe, G. Wang, A. W. Tricker, R. Mukundan, A. Z. Weber and X. Peng, *Joule*, 2024, **8**, 2357–2373.
15 B. Huang, X. Wang, W. Li, W. Tian, L. Luo, X. Sun, G. Wang, L. Zhuang and L. Xiao, *Angew. Chem., Int. Ed.*, 2023, **62**, e202304230.
16 G. Yang, S. Yu, J. Mo, Z. Kang, Y. Dohrmann, F. A. List III, J. B. Green Jr, S. S. Babu and F.-Y. Zhang, *J. Power Sources*, 2018, **396**, 590–598.
17 S. A. Grigoriev, P. Millet, S. A. Volobuev and V. N. Fateev, *Int. J. Hydrogen Energy*, 2009, **34**, 4968–4973.
18 F. Rocha, R. Delmelle, C. Georgiadis and J. Proost, *J. Environ. Chem. Eng.*, 2022, **10**, 107648.
19 M. Bercea, *Polymers*, 2024, **16**, 2021.
20 M. Kurakula and G. K. Rao, *J. Drug Deliv. Sci. Technol.*, 2020, **60**, 102046.
21 R. Vaid, E. Yildirim, M. A. Pasquinelli and M. W. King, *Molecules*, 2021, **26**, 7554.
22 K. Li, Y. Qi, Y. Zhou, X. Sun and Z. Zhang, *Polymers*, 2021, **13**, 573.
23 A. Filimon, A. M. Dobos, M. D. Onofrei and D. Serbezeanu, *Polymers*, 2025, **17**, 1016.
24 D. Patil and S. Madhamshettiwar, *J. Appl. Chem.*, 2014, **2014**, 286709.
25 D. Gonzalez Ortiz, M. Nouxet, W. Maréchal, O. Lorain, A. Deratani and C. Pochat-Bohatier, *Membranes*, 2022, **12**, 664.
26 S. Bonakdar, S. H. Emami, M. A. Shokrgozar, A. Farhadi, S. A. H. Ahmadi and A. Amanzadeh, *Mater. Sci. Eng., C*, 2010, **30**, 636–643.
27 M. J. Park, R. R. Gonzales, A. Abdel-Wahab, S. Phuntsho and H. K. Shon, *Desalination*, 2018, **426**, 50–59.
28 N. Zhang, Y. Pang, Z. Li, C. Yang, L. Zong, H. Yang, H. Wu, Y. Duan and J. Zhang, *Compos. Sci. Technol.*, 2023, **231**, 109801.
29 J. O. Dennis, M. Shukur, O. A. Aldaghri, K. H. Ibnaouf, A. A. Adam, F. Usman, Y. M. Hassan, A. Alsadig, W. L. Danbature and B. A. Abdulkadir, *Molecules*, 2023, **28**, 1781.
30 S. S. Devangamath, B. Lobo, S. P. Masti and S. Narasagoudr, *J. Mater. Sci.: Mater. Electron.*, 2020, **31**, 2904–2917.
31 J. Gilbert, J. Kipling, B. McEnaney and J. Sherwood, *Polymer*, 1962, **3**, 1–10.
32 G. Y. Rudko, A. O. Kovalchuk, V. I. Fediv, W. M. Chen and I. A. Buyanova, *J. Colloid Interface Sci.*, 2015, **452**, 33–37.
33 H. P. Boehm, *Carbon*, 2002, **40**, 145–149.
34 J. L. Figueiredo, M. Pereira, M. Freitas and J. Órfão, *Carbon*, 1999, **37**, 1379–1389.
35 Y.-Q. Wang, F.-Q. Zhang and P. M. Sherwood, *Chem. Mater.*, 1999, **11**, 2573–2583.
36 S. Dong, J. Yan, N. Xu, J. Xu and H. Wang, *Surf. Sci.*, 2011, **605**, 868–874.
37 S. Favero, I. E. Stephens and M. M. Titirci, *Adv. Mater.*, 2024, **36**, 2308238.
38 E. K. Volk, A. L. Clauser, M. E. Kreider, D. D. Soetrisno, S. Khandavalli, J. D. Sugar, S. Kwon and S. M. Alia, *ACS Electrochem.*, 2025, **1**, 239–248.
39 P. Sullivan, D. Dockar and R. Pillai, *J. Chem. Phys.*, 2025, **162**, 184501.
40 C.-H. Zhang, F.-l. Yang, W.-J. Wang and B. Chen, *Sep. Purif. Technol.*, 2008, **61**, 276–286.
41 Y. j. Wu, J. Yang, T. x. Tu, W. q. Li, P. f. Zhang, Y. Zhou, J. f. Li, J. t. Li and S. G. Sun, *Angew. Chem., Int. Ed.*, 2021, **60**, 26829–26836.
42 Y. Jia, L. Zhang, G. Gao, H. Chen, B. Wang, J. Zhou, M. T. Soo, M. Hong, X. Yan and G. Qian, *Adv. Mater.*, 2017, **29**, 1700017.
43 J. Kong, H. Kim and H. S. Park, *Appl. Catal., B*, 2023, **338**, 123019.

